EUROPEAN JOURNAL OF COMPUTATIONAL MECHANICS, 2017
VOL. 26, NOS. 1–2, 172–204
https://doi.org/10.1080/17797179.2017.1306829

Taylor & Francis
Taylor & Francis Group

Advanced computational simulations of water waves interacting with wave energy converters

Ashish Pathak, Cole Freniere and Mehdi Raessi

Department of Mechanical Engineering, University of Massachusetts-Dartmouth, North Dartmouth, MA, USA

ABSTRACT

Wave energy converter (WEC) devices harness the renewable ocean wave energy and convert it into useful forms of energy, e.g. mechanical or electrical. This paper presents an advanced 3D computational framework to study the interaction between water waves and WEC devices. The computational tool solves the full Navier–Stokes equations and considers all important effects impacting the device performance. To enable large-scale simulations in fast turnaround times, the computational solver was developed in an MPI parallel framework. A fast multigrid preconditioned solver is introduced to solve the computationally expensive pressure Poisson equation. The computational solver was applied to two surface-piercing WEC geometries: bottom-hinged cylinder and flap. Their numerically simulated response was validated against experimental data. Additional simulations were conducted to investigate the applicability of Froude scaling in predicting full-scale WEC response from the model experiments.

ARTICLE HISTORY
Received 22 September 2016
Accepted 12 November 2016

KEYWORDS
Multi-phase; fluid–structure interaction; volume-of-fluid; surface piercing; wave energy converter; Froude scaling

1. Introduction

Ocean waves present a vast energy resource that has largely remained untapped. According to the Electric Power Research Institute (Jacobson, Hagerman, & Scott, 2011), the total recoverable wave energy along the U.S. shelf edge is 1170 TWh/yr, which is 30% of the nation's total electricity demand. Drew, Plummer, and Sahinkaya (2009) lists the benefits of harnessing wave energy compared to other energy resources. Among all the renewable energy resources, ocean waves have the maximum energy density and the least environmental impact. Seasonal variability follows the electricity demands. Power can be generated for 90% of the time in contrast to 20–30% in solar and wind devices (Drew et al., 2009). In order to leverage these benefits, substantial research and development effort is still warranted towards making wave energy converter (WEC) devices economically viable and commercially competitive. Folley (2016) details the main reasons behind the slow progress of WEC technology: (1) WEC technologies

CONTACT Mehdi Raessi mraessi@umassd.edu

that exist today have a wide range of design and operating principles, each making a different demand on the numerical modelling technique; (2) being a relatively new field, there is little consensus on a modelling technique for a given WEC design; (3) field data for WECs are scarce because very few have actually been deployed in oceans making it extremely difficult to validate and calibrate a modelling technique. Therefore, in the absence of comprehensive field data, it is crucial to have accurate modelling tools that are applicable to 'real-life' scenarios and capable of making correct predictions of WEC response under realistic conditions. Such tools can then be reliably used to explore a broad range of design space.

In the current work, we present an advanced computational framework that solves the full 3D Navier–Stokes (N-S) equations in multi-phase flows and accurately computes the interaction between waves and WEC devices. Because no simplification is made in the hydrodynamic equations, all important effects influencing the fluid–structure interaction (FSI) are resolved; hence, a wide variety of WEC devices can be simulated. In the present work, we have focused on two devices: bottom-hinged pitching cylinder and flap-type WECs. A clear advantage of bottom-hinged devices is that in the event of a storm they can be made to sink and lay at the sea bottom until calmer conditions prevail (Flocard & Finnigan, 2010), protecting them from extreme wave forces. These devices are designed to operate at nearshore intermediate depths. According to Flocard and Finnigan (2010), nearshore locations offer many advantages: WECs are protected from extreme waves otherwise present in deep oceans; maintenance/installation costs are smaller than in deep seas; compared to shoreline devices, nearshore locations offer higher wave energy density and have negligible visual and environmental impact. We present simulations of bottom-hinged WECs that pierce the water free surface. Flocard and Finnigan (2012) experimentally observed that surface-piercing WEC devices capture 15% more wave power than fully submerged ones. That was attributed to a concentration of wave energy near the water free surface. It is estimated that about 95% of the wave energy is contained within a zone located between the water free surface and a water depth of a quarter of the wavelength (Drew et al., 2009).

The numerical method employed in the current work is similar to the FSI framework presented by Pathak and Raessi (2016a). In the present study, a new multigrid preconditioned pressure Poisson solver is introduced, which reduces the turnaround of large-scale parallel simulations significantly. The organisation of the paper is as follows. An overview of WEC design techniques is delineated in Section 2. Section 3 presents the governing equations. Their numerical implementation is provided in Section 4. In Section 5, the numerical framework is applied to two different types of WECs, where present simulations are compared against published experimental data-sets. The simulations are further used to investigate the applicability of the Froude scaling in predicting the

response of WEC devices in the full scale from the model experiments. Finally, the work is concluded in Section 6.

2. WEC design techniques

Significant engineering time and effort is required for finalising a WEC design before deploying a full-scale WEC prototype in the ocean. This step requires exploring various design spaces and the impact of different design parameters on the power output. Commonly used tools for WEC design development have traditionally been: (1) wave tank experiments with geometrically scaled WEC models and (2) computational tools that are based on the potential flow theory. We shall discuss the range of validity and limitation associated with both approaches.

2.1. Experiments

Wave tank experiments with WEC device models employ Froude's theory, which was originally formulated to compute drag on ships. According to this theory, the total resistance on the ship is composed of wave drag (inertial) and viscous drag (Lewis, 1988):

$$R_T(\text{total}) = R_R(\text{wave}) + R_F(\text{viscous}) \tag{1}$$

First, the total drag $R_{T,\text{model}}$ at a model scale is measured. The viscous resistance $R_{F,\text{model}}$ is estimated using an empirical relation. The residual $R_{R,\text{model}}$ is found by subtraction, $R_{R,\text{model}} = R_{T,\text{model}} - R_{F,\text{model}}$, and then scaled as:

$$R_{R,\text{full}} = R_{R,\text{model}} \cdot \lambda^3 \tag{2}$$

where λ is the geometric Froude length factor. The viscous resistance $R_{F,\text{full}}$ is computed using the same empirical relation as in the model scale. The total drag at the full scale is then predicted as:

$$R_{T,\text{full}} = R_{R,\text{full}} + R_{F,\text{full}} \tag{3}$$

The approach can be justified by considering the N-S equations. Hughes (1993) shows that all the terms in the N-S equations are in similitude under the Froude scaling with the exception of the viscous term. In other words, effects like diffraction and radiation (even nonlinear) can be accurately represented by Froude scaled model experiments.

A basic assumption in the above procedure is that the total force is a linear superposition of independent inertial and viscous forces which follow their individual scaling laws. However, this approach may not always work. For illustration, we consider the work of Sarpkaya (1986), who studied the force on a cylinder due to an oscillating flow. The inertial and viscous drag coefficients,

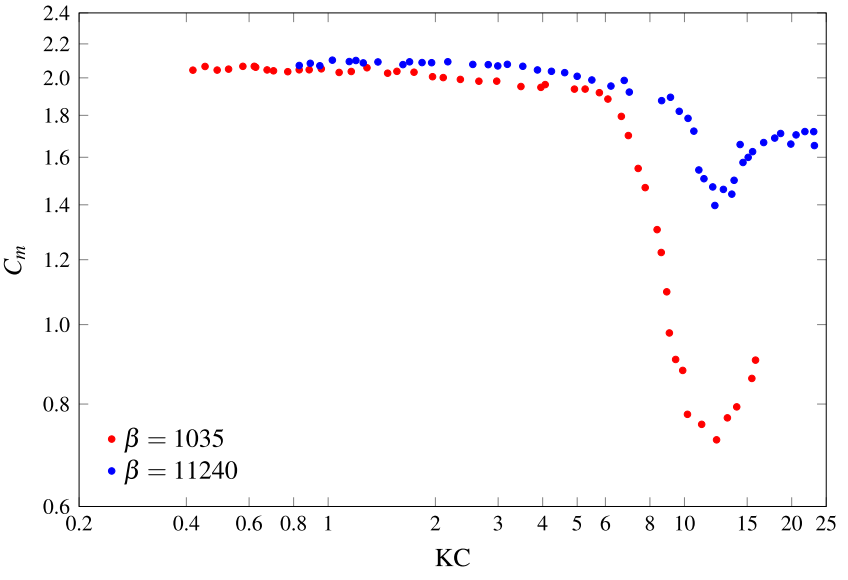

Figure 1. The inertial coeffcient C_m as a function of the Keulegan–Carpenter (KC) number at two β values, corresponding to a Froude length factor of 4.9.
Note: Adopted from Sarpkaya (1986).

represented, respectively by C_m and C_d, were computed as functions of two quantities: the Keulegan–Carpenter number $\mathrm{KC} = U_m T/D$ and $\beta = D^2/\nu T$. Here U_m is the maximum relative velocity between the oscillating flow and the rigid body, D is the cylinder diameter, T is the time period of the oscillating flow and ν denotes the kinematic viscosity. The total force was assumed to be a linear combination of drag and inertial forces (Morison, Johnson, & Schaaf, 1950; Sarpkaya, 1986),

$$F = \frac{1}{2}\rho L D C_d |U| U + \frac{1}{4}\pi \rho D^2 L C_m \frac{\mathrm{d}U}{\mathrm{d}t} \tag{4}$$

where L represents the length of the cylinder, ρ is the fluid density and $U = U_m \cos(2\pi t/T)$. The total force experienced by the cylinder was measured at various KC and β. Coefficients C_d and C_m were computed using Fourier analysis. Figure 1, adopted from Sarpkaya (1986), shows C_m for two values of β and various KC numbers. Suppose the geometric length factor is λ in the Froude scaling, then time scales as $\sqrt{\lambda}$, while KC remains invariant and β scales as $\lambda^{3/2}$. In the example shown in Figure 1, $\lambda = 4.9$, which means that $\beta = 1035$ at the model scale will correspond to $\beta = 11240$ at the full scale. For small KC ($\mathrm{KC} < 6$), C_m is a constant with a value of about 2.0 for both values of β. Consequently, Froude scaling of the inertial forces is valid in that range of KC number. However, at higher KC numbers, C_m at the two scales become significantly different. For example, at $\mathrm{KC} = 10$, $C_m = .81$ at the model scale ($\beta = 1035$) and $C_m = 1.81$ at the full scale ($\beta = 11240$). A Froude scaling of the inertial forces measured at the model scale will result in an error of 135%. This example demonstrates that at

higher KC numbers, viscous effects start affecting the inertial forces and the two are no longer independent. It then becomes difficult for model scale experiments to make reasonably accurate predictions at full scale.

2.2. Potential flow theory

We now consider computational tools for WEC analysis, which are based on the potential flow theory and can be categorized into two groups: (1) frequency domain models and (2) time domain models. The time domain models can be further classified as: (1) Cummins theory-based methods, (2) perturbation-based methods and (3) fully non-linear methods. A detailed discussion of these methods can be found in Folley (2016) and Li and Yu (2012). Here, we provide a brief summary.

2.2.1. Frequency domain models

Frequency domain models are the simplest of all and employ the linearised potential flow equations and boundary conditions. A popular commercial code using this approach is WAMIT (Lee & Newman, 2013). Here, the hydrodynamic force is assumed to be a linear superposition of incident, diffracted and radiated waves. The linear assumption is valid for small amplitude waves and small device motion. For higher waves and larger device motion, e.g. at resonance, the hydrodynamic components start interacting and linear superposition does not hold anymore. Frequency domain models do not support nonlinear terms. They cannot, therefore, model power take off (PTO) damping strategies designed for maximum power extraction that are complex and highly nonlinear.

2.2.2. Time domain models

Time domain models provide a framework to include the nonlinear terms. The simplest models in this category are based on the Cummins method (Cummins, 1962), where the hydrodynamic forces are considered to be linear. These models can simulate more realistic irregular waves, which is a significant improvement over frequency domain models that can handle only monochromatic waves. The complexity of the time domain models can be enhanced by applying perturbation theory. Here, the velocity potential, pressure and the free surface elevation are expressed as perturbation series in wave steepness, ϵ, up to the desired order. Perturbation-based models require wave steepness to be small, $\epsilon << 1$, and the WEC device to have small motions about its equilibrium position.

These limitations are overcome by the fully non-linear potential flow (FNPF) models (Koo & Kim, 2004), through boundary conditions applied on moving surfaces. These models, however, cannot model wave load due to wave breaking around structures that can significantly impact the performance and survivability of a WEC device. In want of a natural dissipation mechanism (viscosity) in the FNPF models, instabilities arising due to large local deformation of water free surface around moving structures may lead to simulation breakdown.

2.2.3. Limitations of potential flow theory

A significant limitation of the models based on the potential flow theory is the assumptions of inviscid and irrotational flow. These assumptions are not generally true for WEC devices that have to undergo large motions to capture a significant portion of wave energy. Potential flow models rely on a quadratic expression borrowed from Morison et al. (1950) to estimate the drag force:

$$F_d = -\frac{1}{2}\rho LDC_d|U_r|U_r \tag{5}$$

Substantial experimental data are needed to carry out Fourier analysis to compute the drag coefficient C_d. Sarpkaya (1976) showed that at high KC numbers (KC $\sim$ 15), the coefficients computed using this approach could not reproduce the measured forces. To achieve a good agreement, additional terms had to be added to Equation (5) by Sarpkaya (1976), and F_d was expressed as:

$$F_d = -\frac{1}{2}\rho LDC_d|U_r|U_r - \frac{1}{2}\rho DLU_m^2\eta C_L \cos(3\theta - \phi) \tag{6}$$

Here, the coefficients in the additional term, namely, ϕ, η and C_L, are computed based on experimental measurements. Equation (6) is not a general expression and is valid only in the neighbourhood of KC $=$ 15. Moreover, at high KC numbers, as mentioned before, the viscous effects start interacting with inertial forces, causing significant deviation from the potential flow predictions.

2.3. Computational fluid dynamics

Computational fluid dynamics (CFD) solvers consider the full N-S equations and therefore can model effects like viscous layer separation, wave breaking and overtopping that may significantly affect the performance of WEC devices. CFD simulations are computationally demanding compared to the potential flow solvers, but recent advancement in computational power and hardware resources has made large-scale CFD simulations feasible. We next present a brief summary on CFD methods that solve FSI involving a water free surface. A detailed discussion on such methods can be found in Haeri and Shrimpton (2012) and Li and Yu (2012). We start with body conformal methods in which the mesh is generated around the structure. Arbitrary Eulerian Lagrangian schemes fall into this category (Farhat, Geuzaine, & Grandmont, 2001). As the structure moves, remeshing is performed in each time step in the entire domain; meshing becomes difficult for arbitrarily complex shaped geometries. Additionally, projecting the solution to the new mesh (remapping) incurs significant overhead cost (Haeri & Shrimpton, 2012). Computationally expensive remeshing/remapping operations can be avoided by using the Immersed boundary (IB) and the fictitious domain (FD) methods, which employ fixed grids. IB methods introduce the effect of solid boundary either by adding a forcing term in the N-S equations (Peskin, 1977) or by imposing a velocity boundary condition in the vicinity of the structure

boundary (Mohd-Yusof, 1997). In the body conformal and the IB methods, the hydrodynamic forces on the structure are computed by explicit integration of pressure and shear around the immersed surface. Hu and Joseph (1992) showed that any scheme employing explicit integration in FSI problems will become unstable if mass of the moving structure is less than the virtual (added) mass of the surrounding fluid accelerated by it. Instabilities arising due to the explicit integration were observed by Fekken (2004) and more recently by Calderer, Kang, and Sotiropoulos (2014). To ensure numerical stability, Hu and Joseph (1992) suggested that the equations of fluid flow and structure motion be solved alternately till a convergence criterion is met. This approach is computationally expensive because each call to the flow solver is time consuming and convergence usually requires several such calls. This iterative procedure can be avoided with the combined weak formulation suggested by Hesla (1991). The method was further developed by Glowinski, Pan, Hesla, and Joseph (1999) who called it the *fictitious domain method*. Later, Patankar, Singh, Joseph, Glowinski, and Pan (2000) and Patankar (2001) made the method fast using conservation of linear and angular momentum. Patankar's approach was then implemented in a finite volume framework by Sharma and Patankar (2005).

In the present work, we have used the fast fictitious domain method of Sharma and Patankar (2005). However, in contrast to the Lagrangian description of the moving structure in their work, we have used a fully Eulerian framework. A fully Eulerian approach offers a number of advantages over a Lagrangian approach, which were presented in Pathak and Raessi (2016a). Discretisation of surface-piercing WECs on an Eulerian mesh involves cells with three phases (solid, water, air), which are resolved using the 3D three-phase interface reconstruction method of Pathak and Raessi (2016b). Including the air phase in the simulation of WECs (and in the solution of the N-S equations) is important; it has been shown by Iafrati, Babanin, and Onorato (2013) that air is responsible for significant energy dissipation during wave breaking via formation of complex dipoles. The water/air flow in the presence of a moving WEC is characterized by high density ratios, which can pose numerical challenges. In this work, a consistent mass and momentum transport scheme (Pathak & Raessi, 2016a; Raessi & Pitsch, 2012) is used to treat such large density ratios and to avoid non-physical interfacial deformation.

3. Governing equations

The two fluids, *fluid 1* and *fluid 2*, interacting with the solid, rigid structure, are assumed to be Newtonian and incompressible. In order to track the three phases in our Eulerian grid, we define two volume-of-fluid (VOF) scalars f and ψ as,

$$f(\vec{x}) = \begin{cases} 1 \ \vec{x} \in fluid1 \\ 0 \ \vec{x} \notin fluid1 \end{cases} \tag{7}$$

$$\psi(\vec{x}) = \begin{cases} 1 \ \vec{x} \in solid \\ 0 \ \vec{x} \notin solid \end{cases} \tag{8}$$

The density and viscosity at any point in the computational domain are defined as,

$$\rho = f\rho_l + \psi\rho_s + (1 - \psi - f)\rho_g \tag{9}$$

$$\frac{1}{\mu} = \frac{f}{\mu_l} + \frac{1-f}{\mu_g} \tag{10}$$

Here, ρ_l, ρ_g denote the densities, and μ_l, μ_g the dynamic viscosities of *fluid 1* and *fluid 2*, respectively. Density of the solid structure is denoted by ρ_s. Equation (10) is applied only on the fluid portion.

The flow field is solved using the continuity and momentum equations:

$$\nabla \cdot \vec{U} = 0 \tag{11}$$

$$\frac{\partial}{\partial t}(\rho\vec{U}) + \nabla \cdot (\rho\vec{U}\vec{U}) = -\nabla p + \nabla \cdot \tau + \vec{F}_B + \vec{F}_{\mathrm{ST}} + \vec{F}_S \tag{12}$$

Here, $\vec{U}$ represents the velocity vector. In Equation (12), $\vec{F}_B$, $\vec{F}_{\mathrm{ST}}$ and $\vec{F}_S$ denote the body force (gravity), the surface tension force and the FSI force, respectively. The pressure and stress tensor are denoted by p and τ, respectively.

The volumes of *fluid 1* and the solid phase are tracked by solving the transport equations of the VOF functions f and ψ:

$$\frac{\partial f}{\partial t} + \vec{U} \cdot \nabla f = 0 \tag{13}$$

$$\frac{\partial \psi}{\partial t} + \vec{U} \cdot \nabla \psi = 0 \tag{14}$$

At the boundaries of the computational domain, with the exception of the wave inlet boundary, we impose no-slip and no-penetration boundary conditions:

$$\vec{U} \cdot \hat{t}_s = 0 \tag{15}$$

$$\vec{U} \cdot \hat{n}_s = 0 \tag{16}$$

A zero pressure gradient is imposed on all domain walls, including the wave inlet boundary.

$$\frac{\partial p}{\partial n_s} = 0 \tag{17}$$

Here, $\hat{n}_s$ and $\hat{t}_s$ are the normal and tangential unit vectors to a domain boundary. The waves are introduced into the computational domain by imposing velocity and surface elevation conditions obtained from the Stoke's theory (Dean & Dalrymple, 1991; Fenton, 1990) at the wave inlet boundary, which is detailed in Section 4.

4. Numerical implementation

The governing equations are discretized using the finite volume method. The discrete equations are solved on a staggered grid where the pressure and VOF scalars are defined at cell centre, while the velocities are defined at cell faces. A detailed explanation of the solution procedure can be found in Pathak and Raessi (2016a, 2016b). In the present work, however, we have used a faster and highly scalable Poisson solver, which is a significant improvement over the Jacobi preconditioned conjugate gradient algorithm used in Pathak and Raessi (2016a). We first provide a brief outline of the solution procedure:

(a) By employing the two-step projection method (Chorin, 1968; Pathak & Raessi, 2016a), Equations (11) and (12) are solved in the entire computational domain after setting the FSI force $\vec{F}_s$ to zero.
(b) The velocity thus yielded is subjected to conservation of linear and angular momentum in the solid region, which is used to obtain rigid body translational and rotational velocities.
(c) The rigid body velocity is imposed inside the solid region. This step is equivalent to applying the FSI force $\vec{F}_s$.

4.1. Consistent transport of three-phase mass and momentum

Figure 2(a) shows the computational domain for modelling a surface-piercing WEC device as an example. Numerical solution of such problems requires the three-phase (liquid, gas, solid) cells to be resolved. A novel VOF-based method detailed in Pathak and Raessi (2016b) is used to perform interface reconstruction and compute mass fluxes in the three-phase cells.

For proper numerical treatment of the fluid flow involving large density ratios, we transport mass and momentum using a consistent scheme. The scheme was first developed by Rudman (1998) and later adopted in three-phase flows by Pathak and Raessi (2016a). Here, the mass and momentum are transported on fine and coarse grids, respectively, as illustrated in Figure 2(b) where the coarse grid is shown with bold lines and the fine grid with thin. As an example, the momentum control volume U is formed by the fine grid cells immediately adjacent to the face on which U resides. The mass flux at the right face of this control volume is computed on the fine grid and is bounded by the shown red box. Since the same mass flux is used to transport both mass and momentum, a tight coupling is established between the two transports. In high density ratio flows, if the mass and momentum are not transported in a consistent manner, the interface may suffer from severe deformations on account of numerically propagated errors (Pathak & Raessi, 2016a; Raessi & Pitsch, 2012).

4.2. Fluid–structure interaction

To capture the FSI, we use the fast fictitious domain method of Sharma and Patankar (2005), which enforces rigidity in the computational cells containing the solid phase. The fictitious domain method involves two stages:

(a) At a time level $n+1$, the velocity $\vec{U}^{n+1}$ yielded by the N-S solver is subjected to linear and angular momentum conservation (in the solid region) , which yields the rigid body translational and rotational velocities, denoted by $\vec{U}_s$ and $\vec{\omega}_s$, respectively, as shown below,

$$M_s \vec{U}_s = \int_{\psi} \rho_s \vec{U}^{n+1} \mathrm{d}v \tag{18}$$

$$I_s \vec{\omega}_s = \int_{\psi} \vec{r} \times \rho_s \vec{U} \mathrm{d}v \tag{19}$$

Here, M_s and ρ_s are the mass and density of the rigid structure, respectively. The volume is denoted by v, and $\vec{r}$ denotes the distance of an infinitesimal volume dv from the centre of mass of the rigid body. The moment of inertia I_s is computed by:

$$I_s = \int_{\psi} \rho_s [(\vec{r} \cdot \vec{r}) I - \vec{r} \otimes \vec{r}] \mathrm{d}v \tag{20}$$

The integrals in Equations (19) and (20) are computed using the 3D geometric toolbox developed by Pathak and Raessi (2016b). A detailed description of the above calculations can be found in Pathak and Raessi (2016a).

(b) In the next step, the rigid body velocity is computed as follows and imposed in the solid region.

$$\vec{U}_{\mathrm{RBM}} = \vec{U}_s + \vec{\omega}_s \times \vec{r} \tag{21}$$

This step is equivalent to applying a FSI force $\vec{F}_s^{n+1}$ in the solid region as:

$$\vec{F}_S^{n+1} = \frac{\rho_s}{\Delta t} \left(\vec{U}_{\mathrm{RBM}}^{n+1} - \vec{U}^{n+1} \right) \tag{22}$$

4.3. The pressure Poisson solver

The discretisation of the pressure Poisson equation (23) leads to a system of linear equations, $Ax = b$, where the divergence of $\vec{U}^*$ and $\vec{F}_{\mathrm{ST}}/\rho$ acts as the source term b, and pressure p is the variable x.

$$-\nabla \cdot \left(\frac{\nabla p^{n+1}}{\rho^{n+1}} \right) = -\frac{1}{\Delta t} \nabla \cdot \vec{U}^* - \nabla \cdot \left(\frac{\vec{F}_{\mathrm{ST}}^{n+1}}{\rho^{n+1}} \right) \tag{23}$$

Two popular methods for solving a large system of linear equations, $Ax = b$, are: (a) the preconditioned conjugate gradient method (PCG) and (b) the

multigrid method. The number of iterations taken by PCG to converge to a fixed tolerance increases with the condition number (κ) of matrix A and the mesh size (Δx) (Volker, 2013). In particular,

$$N_{\text{iters}} \sim \mathcal{O}(\sqrt{\kappa}) \quad \text{and} \quad N_{\text{iters}} \sim \mathcal{O}(1/\Delta x) \tag{24}$$

In multiphase flow applications, condition number κ is a strong function of the density ratio and tends to acquire large values for high density ratio problems (Duffy, Kuhnle, & Sussman, 2012). Compared to the PCG method, the multigrid method shows much faster convergence rate primarily because it can dissipate effectively the low frequency residuals on coarser multigrid levels (Briggs, Henson, & McCormick, 2000). The number of iterations taken by the multigrid method is independent of mesh resolution, unlike in the PCG method. This property makes the multigrid method highly scalable and parallelisable.

The multigrid method, however, may fail to converge if the source term b is oscillating at a high frequency (Ernst & Gander, 2012). In multiphase flows, such condition arises when the free surface is undergoing large deformation. Figure 3 shows an example where a small filament is formed when the water slams against a moving structure. This results in a high frequency oscillation in the source term, which is shown by labels bounded by blue. The example has been taken from Pathak and Raessi (2016a, Section 4.4), where the free roll decay of a rectangular barge was studied.

The PCG method is capable of effectively dissipating such highly oscillating residuals, but its convergence rate is slow due to the slowly decaying low frequency residuals. Tatebe (1993) for the first time combined the CG and the multigrid methods to propose a multigrid preconditioned scheme (MGPCG) that is superior to either method. MGPCG inherited the best properties of MG and PCG methods, which are:

(a) Faster convergence independent of mesh resolution, which leads to scalable and parallelisable algorithm.
(b) More robustness, especially in problems involving a highly oscillating source term, similar to the example shown in Figure 3.

Tatebe (1993) showed that a multigrid preconditioner of CG reduced the condition number (κ) of matrix A by clustering the eigenvalues around a particular value. As a result, the number of iterations taken by CG to converge reduces significantly.

We adopted Tatebe's method in the present work, with a few modifications that are listed below:

(a) The Bi-CGSTAB (Vorst, 1992) was used as the base solver. Although the computational cost is twice that of the CG in each iteration, we found Bi-CGSTAB to be more efficient in reducing the residuals.

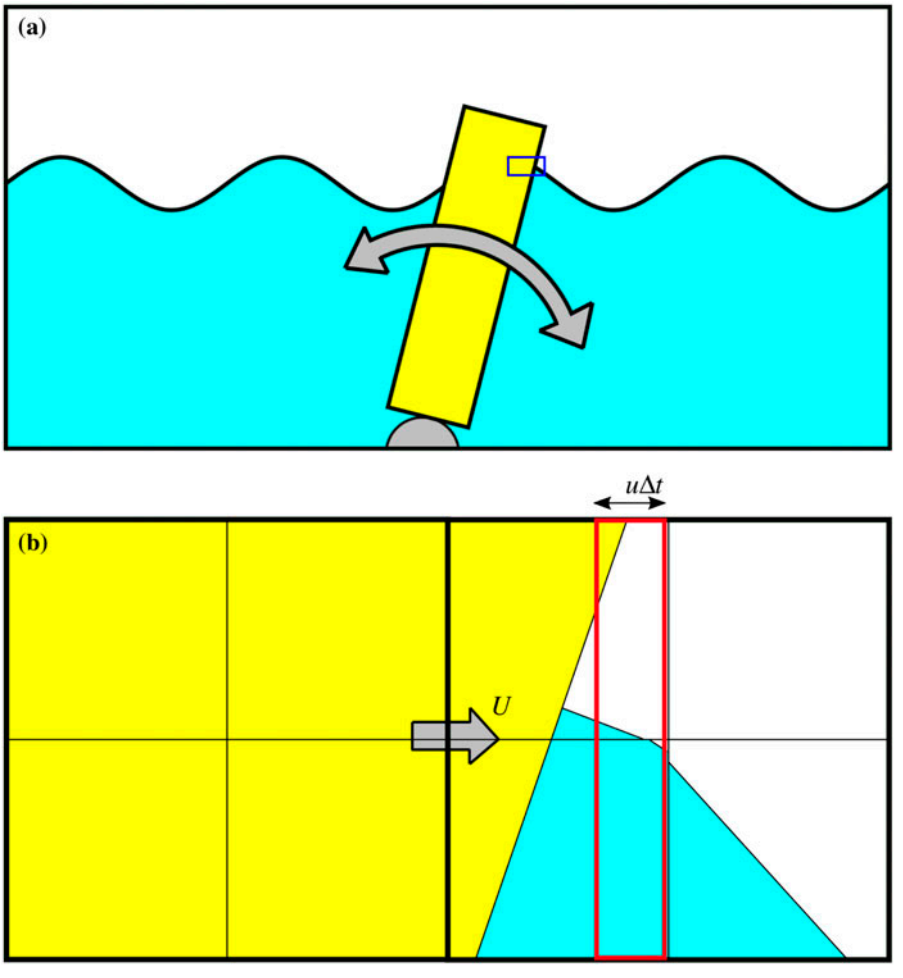

Figure 2. (a) A surface-piercing device pitching in response to waves. The triple point (contact line in 3D) where all three phases, air/water/solid, meet is also shown, along with (b) a magnified view, where the three-phase interface reconstruction and the numerical discretisation are illustrated.
Note: The mass flux at the right face of the U momentum control volume is bounded by red.

(b) The multigrid preconditioner was adopted from BoxLib's library (Bell et al., 2012), that uses Bi-CGSTAB at the coarsest multigrid level. The time spent on Bi-CGSTAB at the coarsest level is insignificant because far less number of cells reside on the coarsest level compared to the regular grid.

The multigrid used in the present work employs a symmetric smoother, RBBR Gauss–Seidel. The restriction operator was regular averaging; the prolongation was its transpose, i.e. piecewise constant interpolation. This particular combination of various components of the multigrid complies with the criteria set forth to act as a preconditioner and ensures convergence (Duffy et al., 2012; Tatebe, 1993). On rare occasions, the bottom Bi-CGSTAB is known to breakdown on account of some coefficients becoming very close to zero. Such oc-

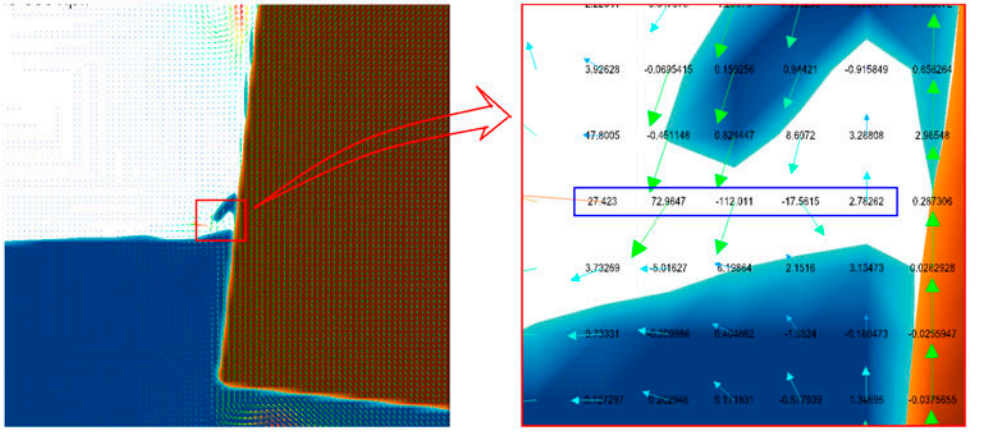

Figure 3. Water filament created due to the water slamming against a rolling rectangular barge (Pathak and Raessi, 2016a).
Notes: The labels represent the divergence of $\tilde{U}^*$ located at cell centre. The region of highly oscillating divergence is bounded by blue box.

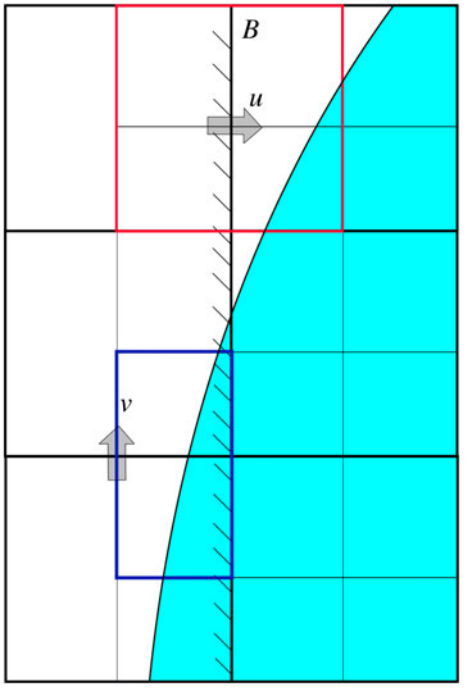

Figure 4. The momentum control volumes near the wave inlet boundary *B*.
Note: The wet control volumes are prescribed a velocity according to the Stokes' second-order wave theory.

currences are identified and the RBBR smoother is utilized at the coarsest level. In Section 5.5.1, the performance of the new MG preconditioned Bi-CGSTAB (MGPBi-CGSTAB) method in handling FSI problems will be assessed.

4.4. Wave generation

The wave generation method used in the present work has been adopted from Jacobsen, Fuhrman, & Fredsøe (2012), and is briefly described here. Consider the boundary *B*, shown by hashed symbols in Figure 4, that acts as a wave inlet to the computational domain. The computational domain (wave tank) lies on the right side of this boundary. The bold and thin lines represent the regular and fine grids, respectively. In the current solver, there is one layer of ghost cells on both fine and coarse grids. The volume fractions of the cells to the right of *B* are computed by the flow solver. On the left, the volume fraction in each fine grid ghost cell is computed based on the analytical free surface elevation and its intersection with the cell. The analytical curve is from the Stokes' second-order wave theory (Fenton, 1990). The velocity control volumes (CVs) for velocity components *u* and *v* have been shown in red and blue, respectively, in Figure 4. The Stokes' theory is used to prescribe the velocity in wet momentum CVs, and a zero velocity is set in dry CVs. The prescribed velocities at the wave inlet *B* act as a time-dependent boundary condition in the solver.

5. Results

In this section, we assess the performance of the computational solver in simulating two different geometries of bottom-hinged WEC devices: a cylinder and a flap. The experimental data-set published in Flocard and Finnigan (2010), Flocard and Finnigan (2012) and Wei, Rafiee, Henry, & Dias (2015) are chosen as the benchmark solutions. First, numerically generated waves are validated against theory and experiments.

5.1. Inlet wave maker

The numerical waves generated using an inlet wave boundary condition are validated with the Stokes' second-order wave theory, and experiments performed by Flocard and Finnigan (2010). Following the experimental conditions (Flocard & Finnigan, 2010, Figure 5), the 'target' waves have a height of $H = 6.3$ cm and a period of $T = 1.25$ s. The wave height is the distance between the wave crest and trough. The simulation used a mesh size of $\Delta x = 5$ mm which equates to 12 cells per wave height. This validation test was run without a WEC, which would otherwise disturb the wave field. Figure 5 shows the numerical free surface elevation compared against the theory and experimental data-sets. The numerical waves require a few periods to reach steady state, after which they are very accurate, and agree well with both theory and experiment. Figure 5(b) shows a magnified comparison between the results. The maximum difference in the numerical and experimental wave heights is less than $.2\Delta x$, which corresponds to .02 H.

5.2. Free pitch decay of a cylinder

The experiments conducted by Flocard and Finnigan (2010) were designed to evaluate the power capture of a pitching cylinder point absorber. The experiments were conducted in a wave flume with a width of 1.0 m. The cylinder had a radius of $R = .1$ m, a height of .725 m and was constrained to rotate about a shaft located 6 cm above the wave tank floor. Free pitch decay experiments were conducted to determine the natural frequency of the cylinder: the cylinder was released from a pitch angle of $\theta = 30°$ in still water, and oscillated until equilibrium. The natural frequency of the cylinder can be calculated through the spectrum of the recorded time history. A water depth of .85 m was used in the numerical simulations in order to fully submerge the cylinder. Mesh resolutions of 20 and 40 cells per diameter (CPD) were employed. As seen in Figure 6, the response at the two resolutions is reasonably close and shows good agreement with the experiment. The 40 CPD results were deemed accurate enough to justify this resolution for simulating the pitch response of the cylinder in waves, which will be presented in Section 5.3.

Figure 7 shows snapshots of the 40 CPD pitch decay simulation at key points in time. Half of the water is made transparent for cylinder's visibility. A plane

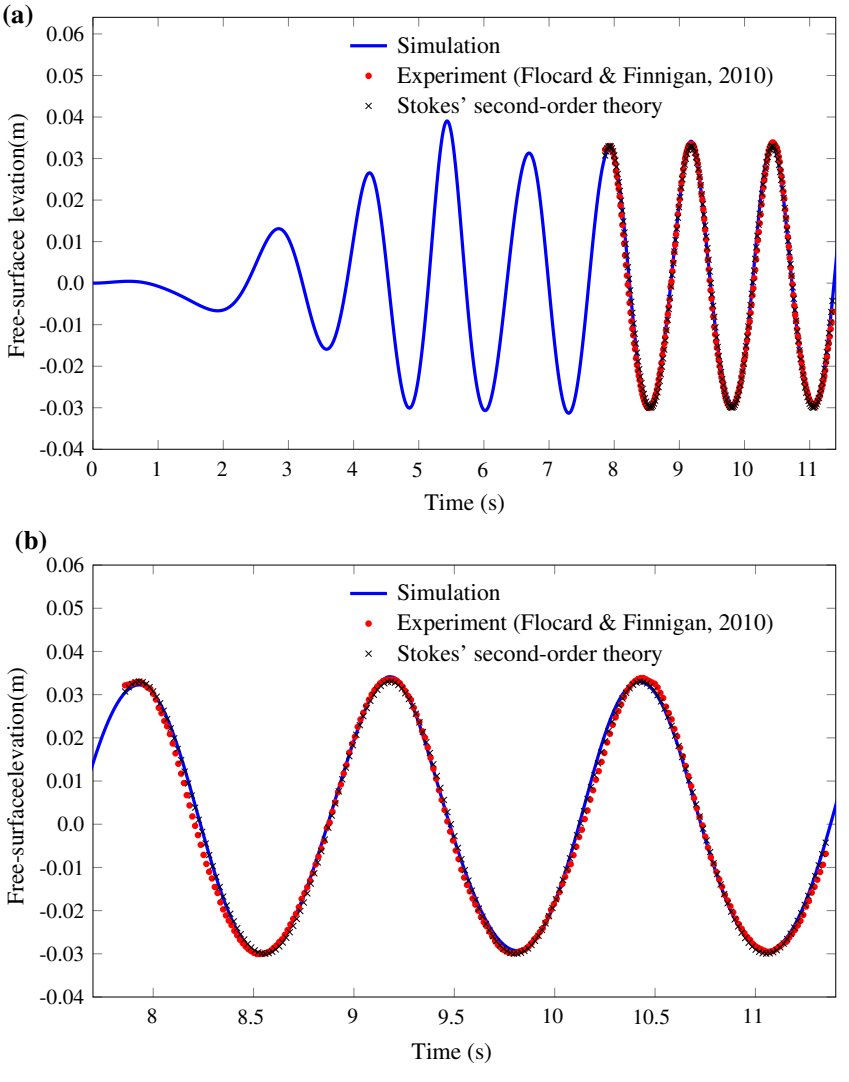

Figure 5. The free surface elevation at a distance of 1.5 wavelengths away from the wave inlet for (a) the full simulation time, and (b) the steady-state response.

located one radius below the tip of the vertical cylinder shows a non-dimensional vorticity field,

$$\omega_z^* = \left((\nabla \times \vec{U}) \cdot \hat{k}\right) D/\bar{U}_{\text{cyl}} \tag{25}$$

where $\bar{U}_{\text{cyl}}$ is the mean velocity of the cylinder tip during its first half period ($\bar{U}_{\text{cyl}} = .7$ m/s). A large vortex forms behind the cylinder initially, and as the cylinder changes direction after .7 s, the vortex scatters into smaller eddies. As the cylinder rises from its initial position, a large cavity is formed on the water free surface (see image at $t = .5$ s). The free surface deformations lead to small breaking waves and air entrapment, which are eventually dispersed.

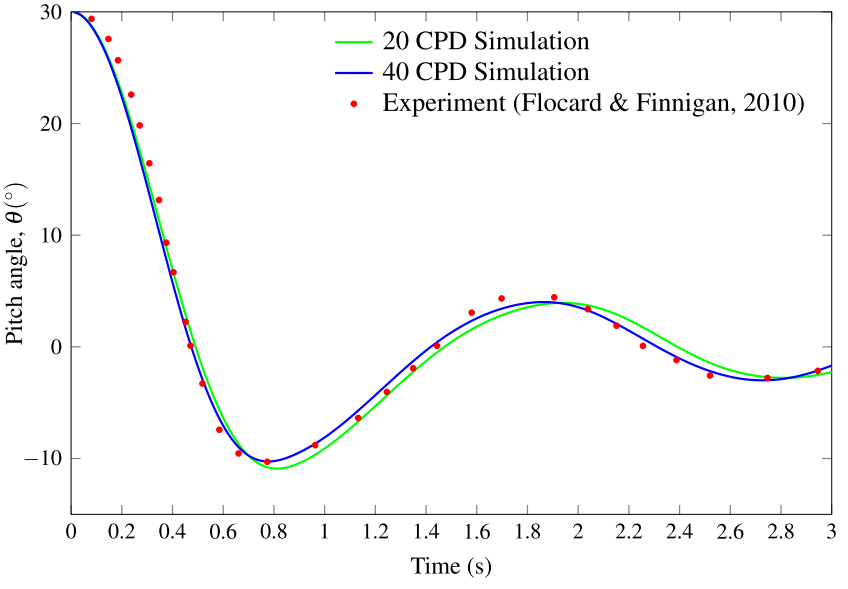

Figure 6. Free pitch decay of a cylinder released from a 30° angle from the vertical.

5.3. *Interaction of a cylinder-type WEC with waves*

In the experimental work of Flocard and Finnigan (2010), the cylinder's pitch response and power capture were measured when subjected to regular waves for a variety of wave heights and frequencies. These waves are well approximated by the Stokes' second-order theory. Wave conditions of $H = 6.3$ cm and $T = 1.56$ s, and a water depth of .7525 m (Flocard & Finnigan, 2010, Figure 5) were chosen for the numerical simulation. The numerical wave tank was 32 m (9 wavelengths) long. The PTO torque was modelled by a linear term:

$$\tau_{\text{PTO}} = -C_{\text{PTO}}\dot{\theta} \tag{26}$$

where $C_{\text{PTO}} = 10$ Nms/rad. Figure 8 shows the simulated cylinder pitching in response to the waves at different times. The extreme and mean cylinder positions in an oscillation period are depicted. Only half the width of water is shown for the cylinder's visibility. The non-dimensional vorticity field is shown on a plane one radius below the tip of the cylinder when it is at its mean position. The velocity used in the non-dimensionalisation of the vorticity field, Equation (25), was the root-mean square (RMS) of the cylinder's tip velocity, oscillating at steady state. A bias can be observed in the distribution of vortices: for waves travelling from left to right, the vortices are concentrated upstream of the cylinder. The vortices dissipate when the cylinder attains the maximum pitch, as seen in Figure 8(c), and reappear when the cylinder pitches back (Figure 8(d)). The evolution of vortex structure is repeated after each time period, which is also visible in similar vortex patterns in Figure 8(a) and (d) that are one period apart. The simulated pitch response in time is quantitatively compared with the experiments in Figure 9.

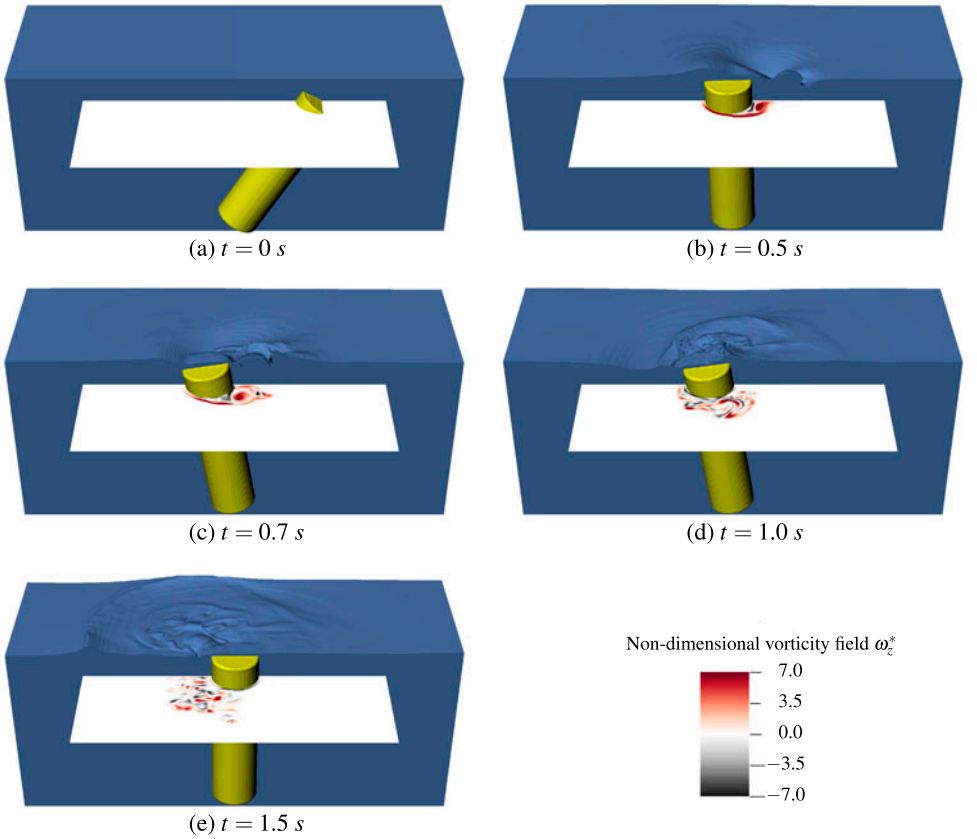

Figure 7. Snapshots of the free pitch decay of a cylinder initially inclined at an angle of 30° in still water.
Note: The non-dimensional vorticity field evolution is shown along a plane at a depth of 14 cm below the mean water level.

There is a clear asymmetry in the experimental results, where the positive pitch angle is approximately 8°, while the negative pitch angle is approximately −6° (see Figure 9(b)). The numerical result on the other hand is nearly symmetric. From Figure 9, it seems that there is a constant shift between the experimental and numerical results. To further investigate this discrepancy, we study a later work by Flocard and Finnigan (2012), which presents extensive experiments on pitching cylinders. In that work, a pitch asymmetry response amplitude operator $RAO\theta_{\text{asym}}$ was introduced to classify the asymmetry of the cylinder under various wave conditions:

$$RAO\theta_{\text{asym}} = (\theta_{\max} + \theta_{\min})D/a_i \tag{27}$$

where D is the diameter of the cylinder, and a_i is the amplitude of the incoming waves. $RAO\theta_{\text{asym}}$ is mainly a function of the wave frequency f_i, the natural frequency f_n of the cylinder, and the wave amplitude a_i (Flocard & Finnigan, 2012). $RAO\theta_{\text{asym}}$ is almost zero when f_i matches f_n (resonance), which is the case in the present simulation, and generally increases in magnitude as $|f_i - f_n|$ increases (Flocard & Finnigan, 2012, Figure 5(b)). The experimental results reported in Flocard and Finnigan (2010), shown in Figure 9, exhibit $RAO\theta_{\text{asym,exp,2010}} = .22$. The present numerical result yields $RAO\theta_{\text{asym,num}} = .04$. However, the experimental results reported in Flocard and Finnigan (2012), which were conducted under nearly identical conditions as in Flocard and Finnigan (2010), exhibit $RAO\theta_{\text{asym,exp,2012}} = .04$, the same value that was obtained in our numerical simulation. In fact, Flocard and Finnigan (2012) reported that $RAO\theta_{\text{asym}} = .22$ is only achieved when the wave frequency and natural frequency of the cylinder are highly disparate, which is not the case in this test problem. Unfortunately, the pitch angle history was not reported by Flocard and Finnigan (2012), and, therefore, a comparison with that work was not possible. Keeping the above discrepancy in mind, the 2010 experiment is still useful for validation because it presents the temporal data for the pitch. If $RAO\theta_{\text{asym, exp, 2012}}$ is used to adjust the 2010 experimental data, then, the numerical and experimental results show excellent agreement (Figure 10).

The instantaneous power extracted by the power-take-off system is $P_{\text{PTO}}(t) = C_{\text{PTO}}\dot{\theta}^2$. Regardless of the above discrepancy in the pitch angle symmetry, the 2010 experimental and the numerical results show an excellent agreement in $\dot{\theta}$, and therefore in P_{PTO} (not shown here).

5.4. Froude scaling of the cylinder's pitch response

The experiments presented by Flocard and Finnigan (2010, 2012) were conducted at the model scale. Froude scaling corresponding to a geometric length scale of $\lambda = 33$ was used to design the cylinder and the wave tank. The experiments were intended to predict the WEC device response at the full scale. With our numerical simulations, we investigated the accuracy with which such predictions can be made. We chose the numerical set-up and wave characteristics presented in the previous test case. But this time we turned off the PTO

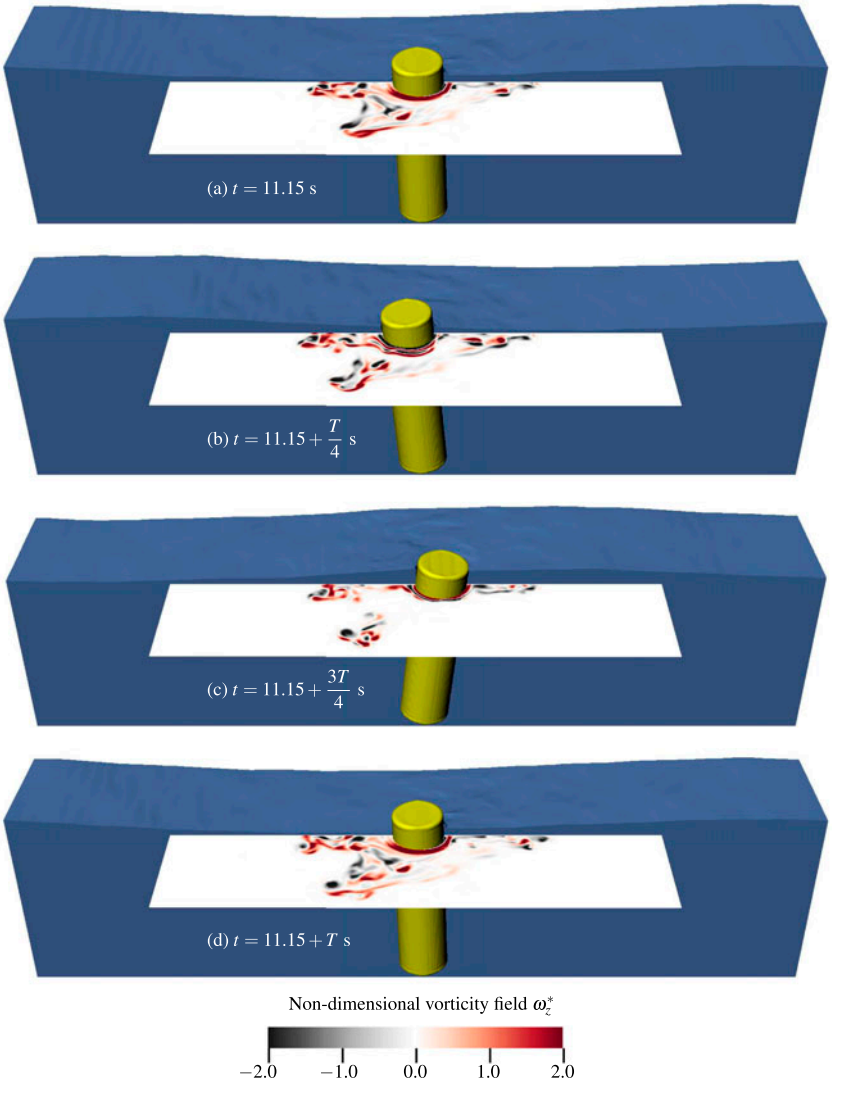

Figure 8. Snapshots of a cylinder-type WEC pitching in response to waves with a height $H = 6.3$ cm and a time period $T = 1.56$ s.
Notes: The non-dimensional vorticity field evolution is shown along a plane at a depth of $R = 10$ cm below the tip of the cylinder at its mean position. Positive denotes a counter clockwise vorticity.

damping to allow higher device velocity relative to the surrounding water. Higher relative velocity translates to a higher KC number and an increasing likelihood of deviating from Froude scaling.

Two simulations, one at model scale and another at full scale (Froude length ratio 1:33), were performed. The pitch responses are shown in Figure 11. The device assumes steady-state oscillations with an amplitude of 12°. The responses obtained at the model and full scales exactly overlap on each other, indicating the validity of Froude scaling. For further insight into the test case, we plotted in Figure 12 the x and z (streamwise and vertical) components of the cylinder

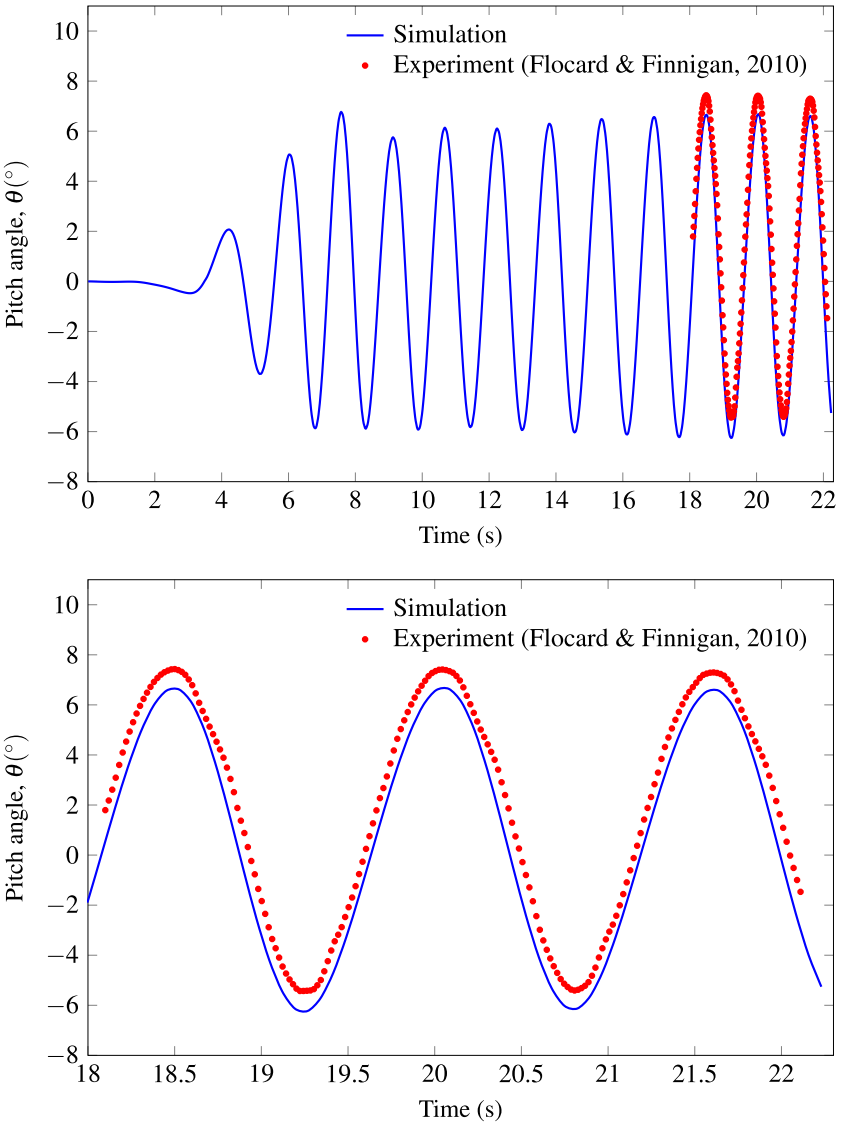

Figure 9. Response of a pitching cylinder interacting with waves of $H = 6.3$ cm and $T = 1.56$ s. The pitch angle is reported for (a) the entire simulation duration, and (b) the steady-state response.

velocity against the corresponding wave velocities. The point on the cylinder located at the mean water level was selected for plotting the device velocity. Analytical expressions from the Stokes' second-order theory were used to plot the wave velocities. The maximum magnitude of the relative velocity between the device and the wave, $|\vec{U}_{\text{device}} - \vec{U}_{\text{wave}}|$ is considered the characteristic velocity U_m in the expression for the KC number, $\text{KC} = U_m T/D$. Following the above approach, it is found that for the present simulation, $\text{KC} = 4.18$. Furthermore, the above simulations verify, for the first time, that the Froude scaling is valid for pitching cylinders in response to waves at $\text{KC} = 4.18$ (or smaller). The validity

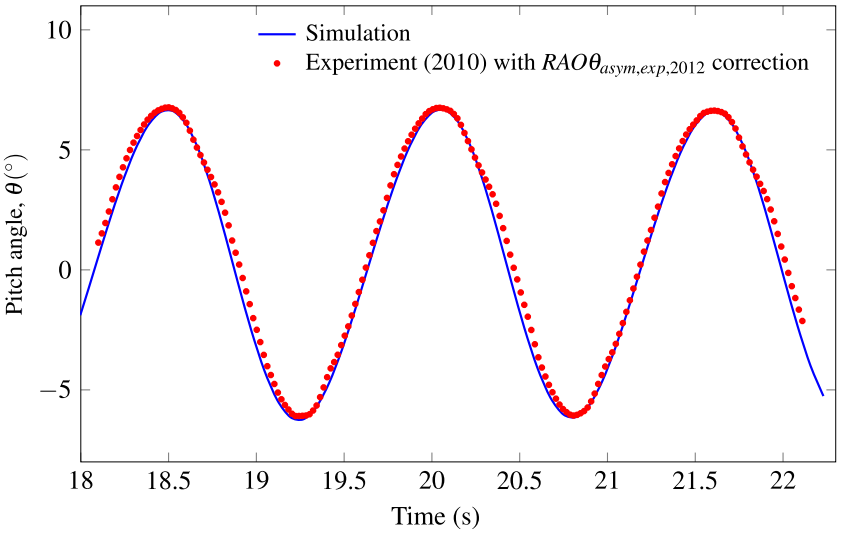

Figure 10. The numerical pitch response of the pitching cylinder is compared with the experimental data of Flocard and Finnigan (2010) that is shifted to reflect $RAO\theta_{\text{asym,exp,2012}}$ reported in Flocard and Finnigan (2012).

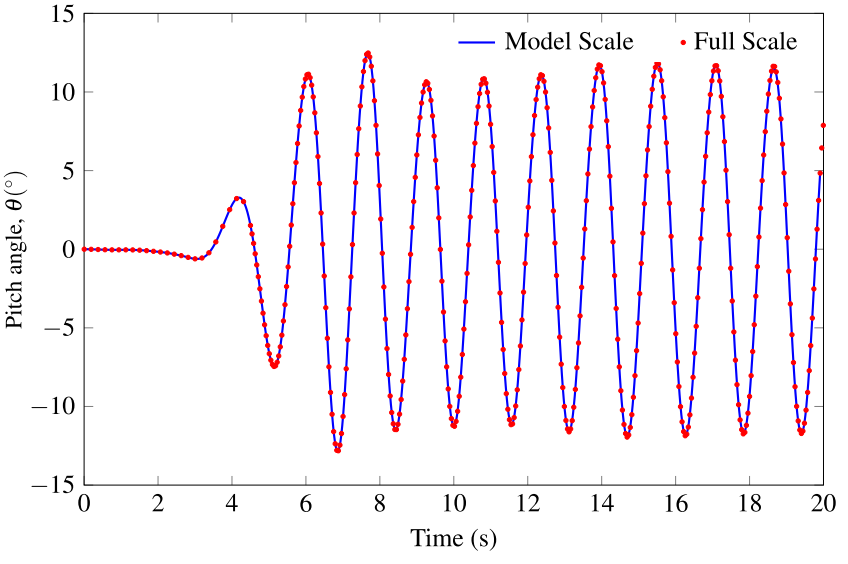

Figure 11. Pitch response of a cylinder at model and full scales is plotted at the model scale.
Notes: Since the Froude length factor $\lambda = 33$, the full scale time was reduced by a factor of $\sqrt{33}$ to make the results at the two scales comparable. The model scale wave characteristics are $H = 6.3$ cm and $T = 1.56$ s.

of Froude scaling at higher KC numbers needs to be verified for this problem. We shall now briefly explain the importance of KC number on the validity of Froude scaling.

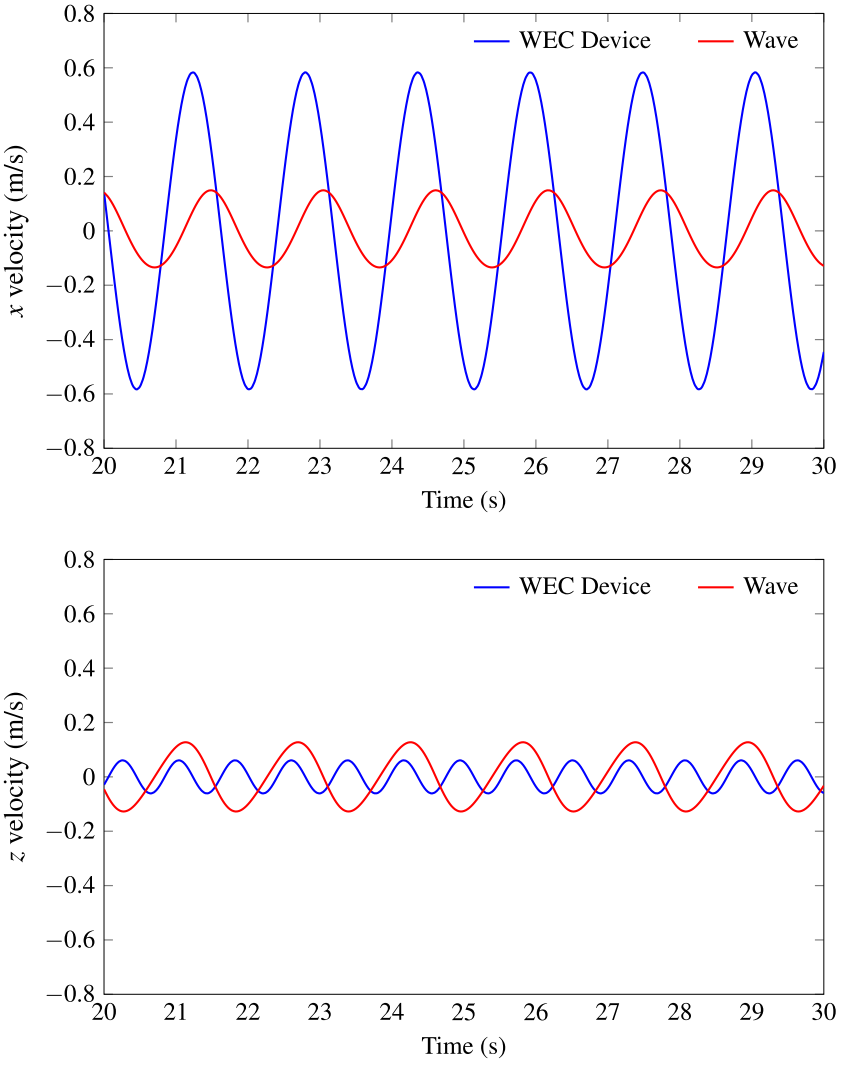

Figure 12. Velocity at a point on the pitching WEC device compared against the Stokes' second-order wave velocity.
Note: The point chosen on the device is located at the mean water level.

5.4.1. Discussion on KC number and Froude scaling

Sarpkaya (1976), in a pioneering work, established that the viscous drag force on a cylinder due to oscillating surrounding fluid flow was a function of KC and β. Under Froude scaling, the KC number remains invariant, but the Reynolds number (and hence β) changes. As a result, viscous effects scale differently than the other (inertial) forces. When viscous effects become important, one would find significant differences between the total force predicted by the Froude-scaled measurements performed on the model scale and the total force actually acting at the full scale. Then, the experimental results at the model scale cannot be relied upon to correctly predict the response at the full scale. Sarpkaya (1986) showed that for various β values, viscous forces start becoming significant relative to

the inertial forces above KC = 10. The KC value of 10 is often cited (Caska & Finnigan, 2008; Wei et al., 2015) and used for WEC devices of various geometries as the point at which the Froude scaling breaks. It is important to note that in Sarpkaya (1986), the rigid body was a fixed fully submerged cylinder exposed to an oscillating cross flow. The effects present in that problem include only the diffraction and the viscous drag. The RMS of the total force was given by Sarpkaya (1986):

$$C_f(r.m.s) = \left(\frac{3}{8}C_d^2 + \frac{\pi^4 C_m^2}{2(\mathrm{KC})^2}\right)^{\frac{1}{2}} \tag{28}$$

where C_d and C_m were the coefficients of drag and inertia, respectively. It can be seen in Equation (28) that the contribution of the inertial term drops sharply as the KC number increases and at KC = 10, the viscous force becomes dominant. In contrast, the problem studied in the present work (as well as in Caska & Finnigan, 2008; Wei et al., 2015) involves a moving object and therefore includes a radiation effect in addition to the diffraction and the viscous effects. As a direct consequence, Equation (28) is not necessarily valid here and the assumption that KC = 10 corresponds to a transition to the viscous regime is a subject of further investigations. The model and full-scale simulations presented above demonstrate that such a transition point is above KC = 4.18. The simulations show that for KC $\leq$ 4.18, the Froude scaling holds, and the model scale experiments can be safely used to extrapolate the WEC behaviour at the full scale. Further research is warranted to identify a KC number above which transition to viscous regime occurs for a cylinder pitching in response to waves.

5.5. Pitch response of a flap-type WEC

In this section, we simulate the pitch response of a flap-type WEC in water waves. The particular test case was borrowed from Wei et al. (2015), which presented results from the experiments conducted in the wave tank facility of the Queen's University, Belfast, Ireland. Figure 13 shows the schematic of the numerical wave tank used in the present simulation. The computational domain size is 28.8 m × 4.608 m × 1.152 m. The water is .691 m deep near the wave inlet boundary located on the left end of the computational domain. The tank floor is not flat and water becomes shallower moving away from the wave inlet. The WEC is a cuboid of size .12 m× 1.04 m × .48 m, and is located in the centre of the tank 7.92 m away from the wave inlet. The tip of the flap WEC is protruding the still water level by .1 m. The WEC is free to pitch about the circular hinge shown in Figure 13. The mass and moment of inertia of the WEC are 33 kg and 1.84 kg m^2, respectively, and the centre of mass is .16 m above the circular hinge. A three-dimensional view of the computational flap, the structure on which it is mounted, and the tank floor are shown in Figure 14. The water waves are generated by imposing a velocity and surface elevation according to the Stokes' theory

(Dean & Dalrymple, 1991) at the wave inlet. The steady-state wave characteristics are $H = .12$ m and $T = 2$ s. The simulation was performed using a uniform mesh that resolves the flap thickness with 10 cells.

Figure 15 shows snapshots of the flap pitching in response to the water waves. Small secondary waves reflected off the flap are visible in the $t = 7.5$ and $t = 7.9$ s images. The pitching angle is plotted in Figure 16, where the simulated result is compared with the experiments. During the transient period, $t < 5$s, an initial forward device motion (negative pitch) can be seen when the waves reach the flap, which is not very well captured by the simulation. That can be attributed to the wave generation methods used in the experiments and simulation, which result in different transient regimes during the initial phase of the problem, a period that is hardly of interest in wave energy conversion. As the time progresses, the simulation shows very good agreement with the experimental pitch data.

Wei et al. (2015) reported experimental data obtained from multiple water height probes. To take a closer look at the free surface dynamics near the WEC, we chose probes 05 and 12 located .9 m in front and .9 m behind the WEC, respectively. The free surface elevations at these probe locations are plotted in Figure 17. At probe 05, the incident wave interacts with the waves radiating away from the flap, which results in a 'double trough'. This effect is captured accurately by the simulation. The small ripples radiating away from the flap can also be seen in the inset provided in Figure 17(a). The simulation is also able to capture the asymmetry in surface elevations about the mean water level.

The results presented in this section demonstrate that the two-way interaction between the waves and the pitching flap is captured very well by the solver. The solver accurately predicts the WEC's pitching motion in response to the water waves as well as the effects of the flap motion on the free-surface dynamics.

5.5.1. The performance of MGPBi-CGSTAB pressure Poisson solver

Here, we assess the acceleration provided by the MGPBi-CGSTAB method that is introduced in this study to solve the pressure Poisson equation. The test problem chosen for this purpose was presented above. The simulation included ~42 million cells and was run on 75 processors. Figure 18 shows the residual history for the MGPBi-CGSTAB and the Jacobi preconditioned conjugate gradient methods. The multigrid preconditioner effectively dissipates the low frequency errors resulting in much faster convergence and shorter run time as evident in the figure. The acceleration factor achieved with MGPBi-CGSTAB is about 24X. The runtime advantage of MGPBi-CGSTAB over PCG becomes even more for large-scale problems with more computational cells due to high scalability and parallelism of the multigrid method.

6. Summary and conclusion

The computational framework presented in this work solves the hydrodynamic equations in the most generalized fashion, capturing all important effects im-

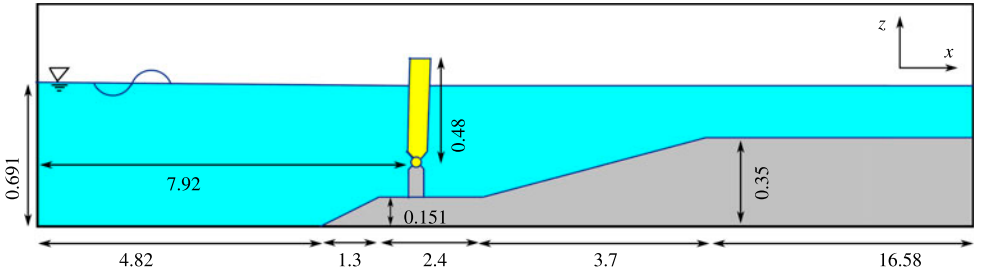

Figure 13. Schematic of the wave tank and the flap-type WEC.
Note: All dimensions are in meters (not to scale). Adopted from Wei et al. (2015).

Figure 14. The flap WEC mounted on a cuboid structure.
Note: Also shown is the sloping floor of the water wave tank.

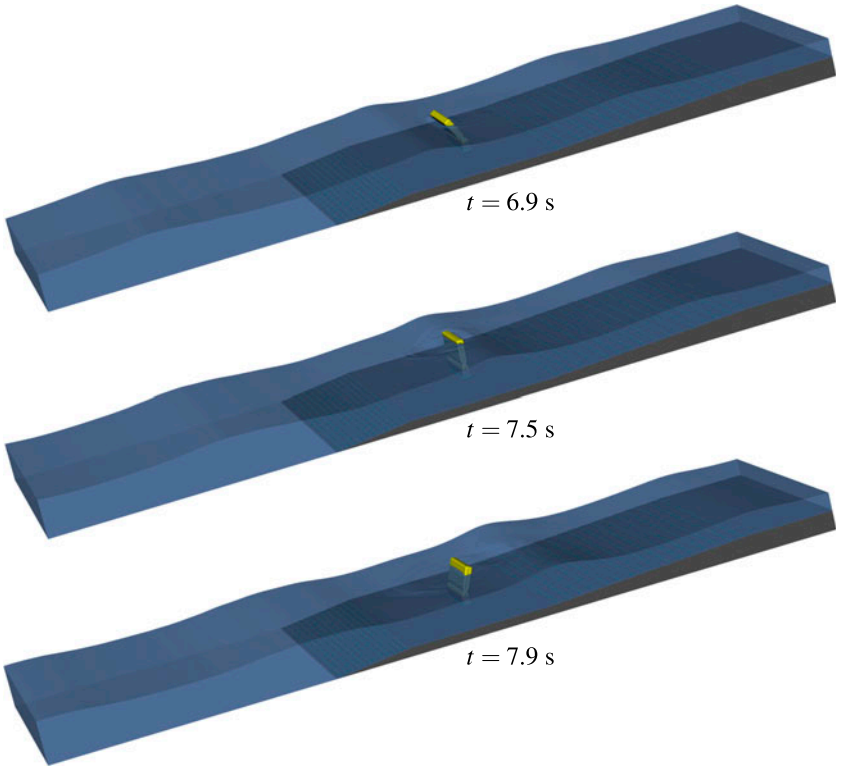

Figure 15. Snapshot of a flap-type WEC pitching in response to waves travelling from left to right.
Note: Water waves have a height of $H = 12$ cm and a time period of $T = 2$ s.

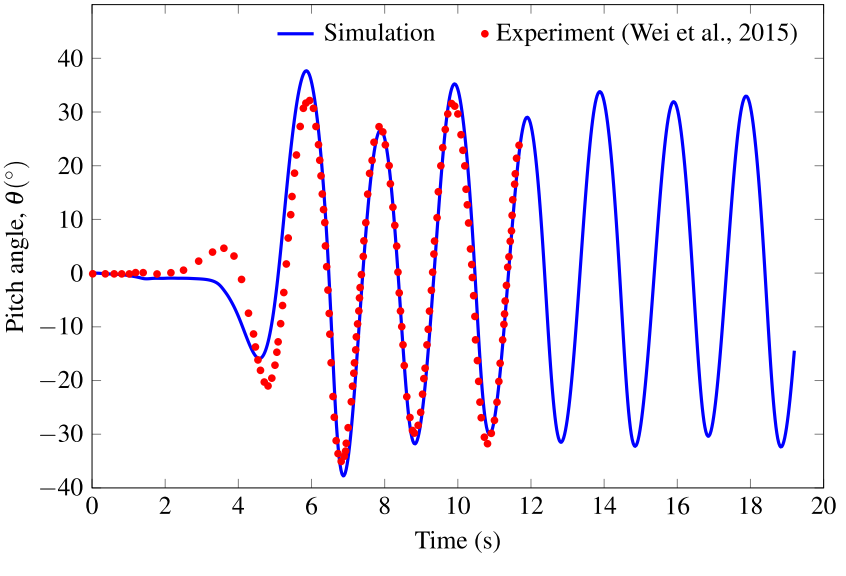

Figure 16. Pitch response of a flap-type WEC in water waves of $H = 12$ cm and $T = 2$ s.

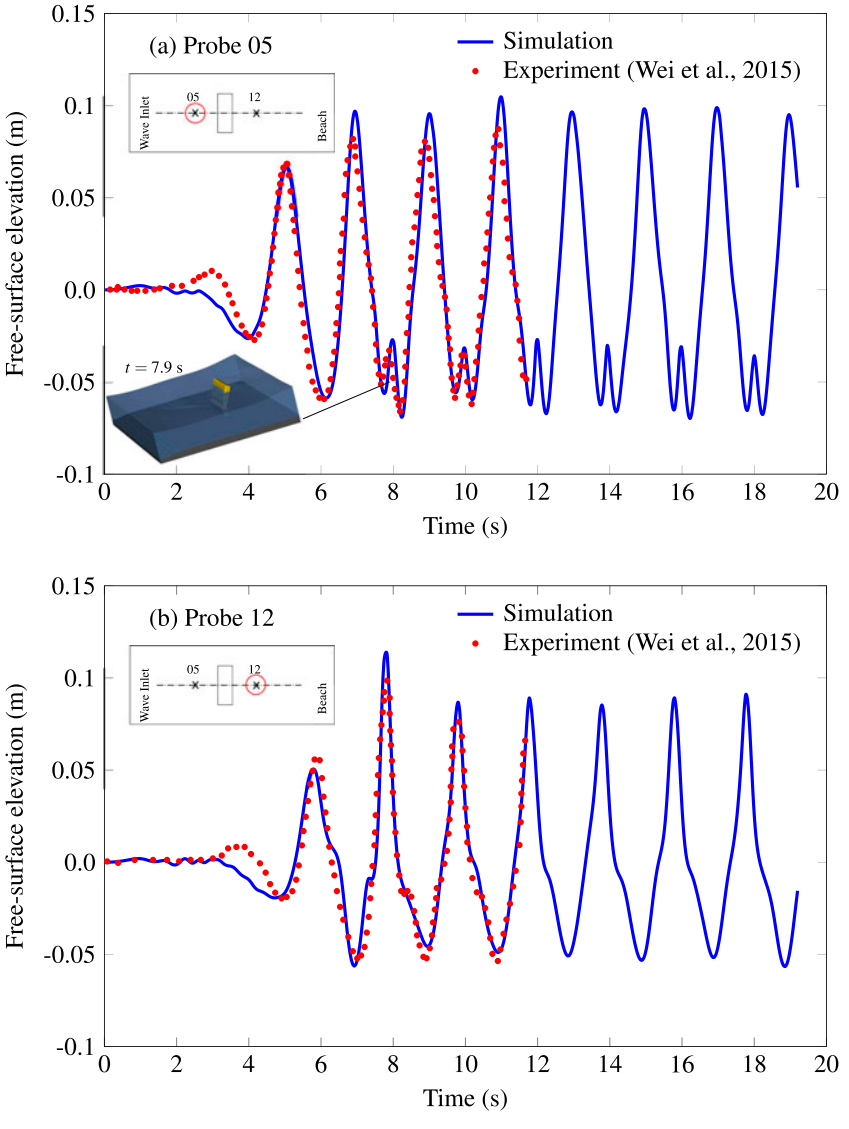

Figure 17. The free surface elevation at (a) probe location 05, and (b) probe location 12.

pacting the dynamics of a WEC device. However, the accuracy of the CFD simulations comes with the burden of high computational costs in order to run at a mesh resolution carrying minimal discretisation errors. With this in mind, the present solver was developed in an MPI parallel environment. The pressure Poisson solver, the computational bottleneck, was accelerated by implementing a multigrid preconditioned Bi-CGSTAB solver, which demonstrated 24X speed-up compared to the Jacobi preconditioned conjugate gradient solver for present simulations. Special numerical schemes were employed to resolve three-phase configurations and handle large density ratios between individual phases.

The computational solver was applied to two different geometries of bottom-hinged pitching devices: cylinder and flap-type WECs. The simulation results

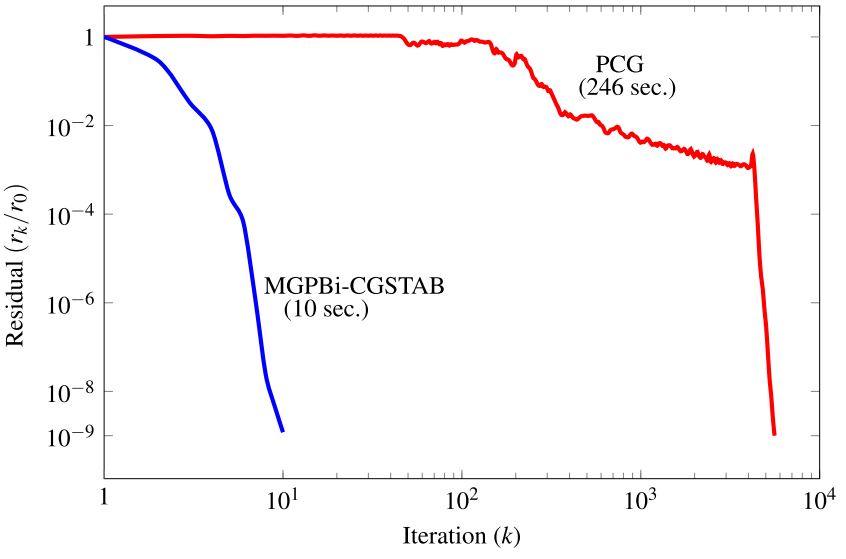

Figure 18. The decay history of the residuals due to the multigrid preconditioned Bi-CGSTAB method and Jacobi preconditioned conjugate gradient (PCG) method.
Note: The wall times spent by the two methods are shown in parentheses.

showed excellent agreement with published experimental data. The experiments were conducted at model scales and were intended to predict, by Froude scaling, the response of the full-scale WECs in the ocean. Additional simulations demonstrated the validity of Froude scaling on pitching cylinders when KC $\leq$ 4.2. Further computational studies are needed to determine the KC value, at which Froude scaling breaks.

Acknowledgements

AP gratefully acknowledges the Fellowship from the Office of the Associate Provost for Graduate Studies at UMass Dartmouth.

Disclosure statement

No potential conflict of interest was reported by the authors.

Funding

The research support from the National Science Foundation (Division of Chemical, Bioengineering, Environmental, and Transport Systems) under the CBET [grant number 1236462], [grant number 1336232] is gratefully acknowledged. The simulations presented here were performed on the UMass Dartmouth HPC cluster, which was purchased through partial support from the NSF [MRI grant number CNS-0959382] and AFOSR [DURIP grant number FA9550-10-1-0354].

References

Bell, J., Almgren, A., Beckner, V., Day, M., Lijewski, M., Nonaka, A., & Zhang, W. (2012). *BoxLib users guide*. Retrieved from https://ccse.lbl.gov/BoxLib/BoxLibUsersGuide.pdf

Briggs, W., Henson, V., & McCormick, S. (2000). *A multigrid tutorial*. Philadelphia (PA): SIAM.

Calderer, A., Kang, S., & Sotiropoulos, F. (2014). Level set immersed boundary method for coupled simulation of air/water interaction with complex floating structures. *Journal of Computational Physics, 277*, 201–227.

Caska, A., & Finnigan, T. (2008). Hydrodynamic characteristics of a cylindrical bottom-pivoted wave energy absorber. *Ocean Engineering, 35*, 6–16.

Chorin, A. J. (1968). Numerical solution of the Navier–Stokes equations. *Mathematics of Computation, 22*, 745–762.

Cummins, W. E. (1962). *The impulse response function and ship motions* (No. DTMB-1661). Washington, DC: David Taylor Model Basin.

Dean, R. G., & Dalrymple, R. A. (1991). *Water wave mechanics for engineers and scientists*. Singapore: World Scientific.

Drew, B., Plummer, A. R., & Sahinkaya, M. (2009). A review of wave energy converter technology. *Proceedings of the Institution of Mechanical Engineers, Part A: Journal of Power and Energy, 223*(8), 887–902.

Duffy, A., Kuhnle, A., & Sussman, M. (2012). *An improved variable density pressure projection solver for adaptive meshes*. Unpublished. Retrieved from http://www.math.fsu.edu/~sussman/MGAMR.pdf

Ernst, O. G., & Gander, M. J. (2012). Why it is difficult to solve helmholtz problems with classical iterative methods. In *Numerical analysis of multiscale problems* (pp. 325–363). Berlin: Springer.

Farhat, C., Geuzaine, P., & Grandmont, C. (2001). The discrete geometric conservation law and the nonlinear stability of ale schemes for the solution of flow problems on moving grids. *Journal of Computational Physics, 174*, 669–694.

Fekken, G. (2004). Numerical simulation of free-surface flow with moving objects (Ph.D. thesis). University of Groningen, Groningen, The Netherlands. Retrieved March, from http://www.ub.rug.nl/eldoc/dis/science/g.fekken

Fenton, J. D. (1990). *Nonlinear wave theories. The Sea, 9*, 3–25.

Flocard, F., & Finnigan, T. (2010). Laboratory experiments on the power capture of pitching vertical cylinders in waves. *Ocean Engineering, 37*, 989–997.

Flocard, F., & Finnigan, T. (2012). Increasing power capture of a wave energy device by inertia adjustment. *Applied Ocean Research, 34*, 126–134.

Folley, M. (Ed.). (2016). *Numerical modelling of wave energy converters*. Amsterdam: Elsevier.

Glowinski, R., Pan, T.-W., Hesla, T. I., & Joseph, D. D. (1999). A distributed Lagrange multiplier/fictitious domain method for particulate flows. *International Journal of Multiphase Flow, 25*, 755–794.

Haeri, S., & Shrimpton, J. S. (2012). On the application of immersed boundary, fictitious domain and body-conformal mesh methods to many particle multiphase flows. *International Journal of Multiphase Flow, 40*, 38–55.

Hesla, T. (1991). *The dynamical simulation of two-dimensional fluid/particle systems*. Unpublished notes

Hu, H. H., & Joseph, D. D. (1992). Direct simulation of fluid particle motions. *Theoretical and Computational Fluid Dynamics, 3*, 285–306.

Hughes, S. A. (1993). *Physical models and laboratory techniques in coastal engineering* (Vol. 7). Singapore: World Scientific.

Iafrati, A., Babanin, A., & Onorato, M. (2013). Modulational instability, wave breaking, and formation of large-scale dipoles in the atmosphere. *Physical Review Letters, 110*, 184504-1–184504-5.

Jacobsen, N. G., Fuhrman, D. R., & Fredsøe, J. (2012). A wave generation toolbox for the open-source CFD library: OpenFoam. *International Journal for Numerical Methods inFluids, 70*, 1073–1088.

Jacobson, P. T., Hagerman, G., & Scott, G. (2011). *Mapping and assessment of the United States ocean wave energy resource* (Technical Report). Paulo Alto: Electric Power Research Institute.

Kim, M.-H., & Yue, D. K. (1989). The complete second-order diffraction solution for an axisymmetric body. Part 1. Monochromatic incident waves. *J. Fluid Mech, 200*, 235–264.

Koo, W. C., & Kim, M. H. (2004). Freely floating body simulation by a 2D fully nonlinear numerical wave tank. *Ocean Engineering, 31*, 2011–2046.

Lee, C., & Newman, J. (2013). Wamit user manual (Version 7.0). Chestnut Hill, MA: WAMIT.

Lewis, E. V. (1988). *Principles of naval architecture second revision* (p. 2). Jersey City, NJ: SNAME.

Li, Y., & Yu, Y.-H. (2012). A synthesis of numerical methods for modeling wave energy converter-point absorbers. *Renewable and Sustainable Energy Reviews, 16*, 4352–4364.

Mohd-Yusof, J. (1997). Combined immersed-boundary/B-spline methods for simulations of flow in complex geometries. *Annual Research Briefs. NASA Ames Research Center, Stanford University Center of Turbulence Research, Stanford*, 317–327.

Morison, J., Johnson, J., & Schaaf, S. (1950). The force exerted by surface waves on piles. *Journal of Petroleum Technology, 2*, 149–154.

Patankar, N. (2001). A formulation for fast computations of rigid particulate flows. *Center for Turbulence Research Annual Research Briefs, 2001*, 185–196.

Patankar, N. A., Singh, P., Joseph, D. D., Glowinski, R., & Pan, T. W. (2000). A new formulation of the distributed Lagrange multiplier/fictitious domain method for particulate flows. *International Journal of Multiphase Flow, 26*, 1509–1524.

Pathak, A., & Raessi, M. (2016a). A 3D, fully Eulerian, VOF-based solver to study the interaction between two fluids and moving rigid bodies using the fictitious domain method. *Journal of Computational Physics, 311*, 87–113.

Pathak, A., & Raessi, M. (2016b). A three-dimensional volume-of-fluid method for reconstructing and advecting three-material interfaces forming contact lines. *Journal of Computational Physics, 307*, 550–573.

Peskin, C. S. (1977). Numerical analysis of blood flow in the heart. *Journal of Computational Physics, 25*, 220–252.

Raessi, M., & Pitsch, H. (2012). Consistent mass and momentum transport for simulating incompressible interfacial flows with large density ratios using the level set method. *Computers and Fluids, 63*, 70–81.

Rudman, M. (1998). A volume tracking method for incompressible multifluid flows with large density variations. *International Journal for Numerical Methods in Fluids, 28*, 357–378.

Sarpkaya, T. (1976). *Vortex shedding and resistance in harmonic flow about smooth and rough circular cylinders at high Reynolds numbers* (Technical Report). Monterey, CA: Naval Postgraduate School.

Sarpkaya, T. (1986). Force on a circular cylinder in viscous oscillatory flow at low Keulegan–Carpenter numbers. *Journal of Fluid Mechanics, 165*, 61–71.

Sharma, N., & Patankar, N. A. (2005). A fast computation technique for the direct numerical simulation of rigid particulate flows. *Journal of Computational Physics, 205*, 439–457.

Tatebe, O. (1993). The multigrid preconditioned conjugate gradient method. In *6th Copper Mountain Conference on Multigrid Methods* (pp. 621–634). Copper Mountain, CO: NASA, Langley Research Center.

Volker, J. (2013). *Multigrid methods*. University Lecture. Retrieved from https://www.wias-berlin.de/people/john/LEHRE/MULTIGRID/multigrid.pdf

Vorst, H. V. D. (1992). A fast and smoothly converging variant of Bi-CG for the solution of nonsymmetric linear systems. *SIAM Journal on Scientific and Statistical Computing, 13*, 631–644.

Wei, Y., Rafiee, A., Henry, A., & Dias, F. (2015). Wave interaction with an oscillating wave surge converter, Part I: Viscous effects. *Ocean Engineering, 104*, 185–203.